

# Correlating Magneto-Structural Properties to Hyperthermia Performance of Highly Monodisperse Iron Oxide Nanoparticles Prepared by a Seeded-Growth Route

Michael Levy,<sup>†</sup> Alessandra Quarta,<sup>‡</sup> Ana Espinosa,<sup>§</sup> Albert Figuerola,<sup>\*,||,⊥</sup> Claire Wilhelm,<sup>†</sup> Mar García-Hernández,<sup>§</sup> Alessandro Genovese,<sup>||</sup> Andrea Falqui,<sup>||</sup> Damien Alloyeau,<sup>#</sup> Raffaella Buonsanti,<sup>‡</sup> Pantaleo Davide Cozzoli,<sup>‡,▽</sup> Miguel Angel García,<sup>\*,○,◆</sup> Florence Gazeau,<sup>†</sup> and Teresa Pellegrino<sup>‡,||</sup>

<sup>†</sup>Laboratoire Matière et Systèmes Complexes (MSC), UMR 7057, CNRS and Université Paris Diderot, 10 rue Alice Domon et Léonie Duquet, 75205 Paris cedex 13, France

<sup>‡</sup>National Nanotechnology Laboratory (NNL), Istituto Nanoscienze-CNR, via per Arnesano 16 Km.5, 73100 Lecce, Italy

<sup>§</sup>Instituto de Ciencia de Materiales de Madrid, Consejo Superior de Investigaciones Científicas, Cantoblanco, Sor Juana Inés de la Cruz 3, 28049 Madrid, Spain

<sup>||</sup>Istituto Italiano di Tecnologia, via Morego 30, 16169 Genoa, Italy;

<sup>⊥</sup>Departament de Química Inorgànica, Universitat de Barcelona, Martí i Franqués 1-11, 08028 Barcelona, Spain

<sup>#</sup>Laboratoire Matériaux et Phénomènes Quantiques (MPQ), UMR 7162, CNRS and Université Paris Diderot, 10 rue Alice Domon et Léonie Duquet, 75205 Paris cedex 13, France

<sup>▽</sup>Dipartimento di Ingegneria dell'Innovazione, Università del Salento, Via per Arnesano, 73100 Lecce, Italy

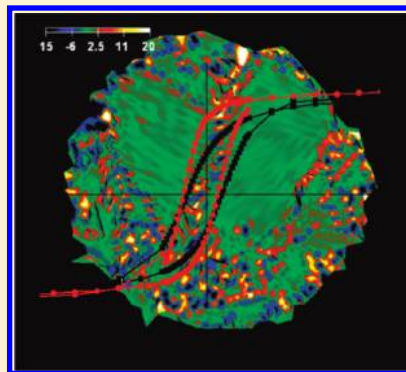
<sup>○</sup>Instituto de Cerámica y Vidrio, CSIC and IMDEA Nanociencia, 28049 Madrid, Spain

<sup>◆</sup>Departamento de Física de Materiales, Universidad Complutense de Madrid, 28040 Madrid, Spain

**S** Supporting Information

**ABSTRACT:** Monodisperse cubic spinel iron oxide magnetic nanoparticles with variable sizes were prepared following a multi-injection seeded-growth approach. As expected from such a well-known synthetic route, all samples were characterized by narrow size distributions, and showed excellent stability in both organic and aqueous media without the presence of aggregates, thus becoming ideal candidates for the study of their hyperthermia performance. Specific Loss Power measurements indicated low heating powers for all samples without a maximum for any specific size, contrary to what theory predicts. The magnetic study showed the formation of size-dependent nonsaturated magnetic regions, which enlarged with the particle size, evidencing a clear discrepancy between the crystal size and the effective magnetic volume. Strain map analysis of high resolution transmission electron micrographs indicated the presence of highly strained crystal areas even if nanoparticles were monocrystalline. The origin of the crystal strain was found to be strictly correlated with the seeded-growth synthetic procedure used for the preparation of the nanoparticles, which turned out to alter their magnetic structure by creating antiphase boundaries. Considering the calculated effective magnetic volumes and their magnetic dispersions in each sample, a reasonable agreement between hyperthermia experiments and theory was obtained.

**KEYWORDS:** iron oxide nanoparticles, thermodecomposition colloidal synthesis, seeded-growth, hyperthermia, magnetic properties, antiphase boundaries, strain analysis



## INTRODUCTION

Controlled heat generation has been devised since years as an efficient way to fight cancer.<sup>1</sup> However, heat should be selectively delivered to the tumor area in order to avoid overheating of healthy tissues in the body. Nanotechnology has provided thermal probes which are more selective toward tumoral cells due to the nanometric dimensions of the particles employed as heating agents. Their nanoscaled sizes, well below the cell dimensions, are promising features for achieving targeted delivery and efficient

cell loading. Magnetic nanoparticles (MNPs), such as of iron oxide, have the capability to release heat under the stimulation of an alternating magnetic field.<sup>2,3</sup> Unlike their use in diagnostics as contrast agents for magnetic resonance imaging (MRI),<sup>4</sup> the clinical use of MNPs for thermal therapy is just in its infancy.<sup>5</sup>

**Received:** April 14, 2011

**Revised:** July 26, 2011

**Published:** September 01, 2011

One of the key limitations for their clinical application deals with the fact that quite large doses are still required to generate an amount of heat sufficient to induce tumor regression. This could be due to the poor colloidal stability and thus to the low amount of magnetic material able to reach the tumoral site through the bloodstream.<sup>6,7</sup> However, in many cases, in addition to the in vivo stability issue, the problem is mainly associated with the inherently low heat generating properties of the MNPs. The specific loss power (SLP) is the parameter quantifying the heating power generated by MNPs and is expressed in W per g of magnetic material. In addition to iron oxide, other materials such as metals would definitely offer higher SLP values. Nevertheless, their use in medicine is strongly limited by their high toxicity.<sup>8</sup> Hence, the understanding of the ideal characteristics of iron oxide MNPs for enhanced heat generation is still a subject of great interest. Even if theory predicts SLP values of up to  $1 \text{ kW g}^{-1}$  for iron oxide MNPs,<sup>2,9,10</sup> such values have rarely been measured experimentally<sup>11</sup> as they often reach only a few hundreds of  $\text{W g}^{-1}$  or even less.<sup>12–15</sup>

In the past decades several studies have been undertaken to correlate the various structural and magnetic features with the hyperthermia performance of iron oxide MNPs. Among these, the size of the particles and their size distribution,<sup>9,12,16</sup> their crystallinity, chemical composition,<sup>10,14</sup> and interparticle interactions<sup>13,17–19</sup> are those intrinsically associated to the magnetic material. Besides these, other aspects such as the physiological conditions or the magnetic field amplitude and frequency used in the measurement appear to be also determinant factors.<sup>20,21</sup> Natural magnetosomes produced by magnetotactic bacteria have so far shown the highest values of SLP, even if their large-scale availability is hard to achieve.<sup>22</sup> Alternatively, iron oxide MNPs can be obtained by a wide variety of synthetic methods, including procedures based on coprecipitation in aqueous media<sup>23–25</sup> or thermal decomposition of molecular precursors in organic solvents.<sup>26–29</sup> To date, almost all studies have focused on iron oxide particles prepared by coprecipitation of di/trivalent iron salts in basic aqueous medium. Actually, commercially available iron oxide nanoparticles for MRI applications are exclusively prepared by this method.<sup>4</sup> Even if the coprecipitation approach remains an economical route to synthesize large amounts of nanostructured iron oxide particles, it also entails several disadvantages in terms of poor degree of size control, crystallinity and colloidal stability. The theoretical model for heating power of single crystal MNPs predicts a sharp maximum for a well-defined diameter (at a given frequency) and a rapid decrease of the SLP when the particle size differs by only one nanometer with respect to the ideal size.<sup>2,9,10</sup> Therefore, a tight control of the particle size and size dispersion appears to be the preliminary most important prerequisite to optimizing the heating power of nanomagnets. In this scenario, the high temperature decomposition of organometallic precursors or metal complexes in mixtures of organic solvents and/or surfactants represents a powerful alternative for the synthesis of aggregation-free MNPs with a high degree of control over size, shape, size dispersion, and crystallinity.<sup>30,31</sup> Several authors have also reported on the enhanced magnetic properties of MNPs prepared by these methods compared to those prepared by coprecipitation procedures.<sup>32,33</sup> Among the numerous variants of the thermal decomposition route, the seeded-growth method has been demonstrated to lead to high-quality nanoparticles with finely tunable sizes and excellent monodispersity for a wide range of materials.<sup>29,30</sup> Consequently, MNPs of certain sizes prepared by this method could, in principle, be ideal candidates to reach

the high SLP values predicted. However, the magnetic characteristics of MNPs prepared by seeded-growth approaches have rarely been studied in detail. MNPs of small enough sizes may suffer from surface effects<sup>34–36</sup> and can also show certain degree of magnetic disorder strictly linked to the synthetic protocol used for their preparation, which can easily degrade their magnetic performance. Hence, the establishment of a correlation between the synthetic method chosen and the magnetostructural characteristics of MNPs thereof represents a fundamental step toward a better understanding of magnetic phenomena in nanoparticles and for the validation of a specific synthetic route to high-quality iron oxide MNPs suitable to be exploited in hyperthermia therapy.

In this manuscript we present an in-depth structural and magnetic characterization of iron oxide MNPs of variable sizes and narrow size variances. All samples were prepared by a surfactant-assisted thermal decomposition approach in organic solvents based on a seeded-growth technique.<sup>29</sup> The presence of amphiphilic surfactant molecules in the reaction mixture was essential to guarantee attainment of unaggregated highly monodisperse particles, with high solubility in nonpolar solvents. The MNPs were further transferred to saline aqueous buffer solution by using a well-established polymer coating process, after which the colloidal stability of the particles was still preserved.<sup>37</sup> The hyperthermia performances of both surfactant and polymer-coated MNPs was examined. We aimed at elucidating the structural and magnetic factors responsible for the low SLP values measured for such samples in an attempt to fully correlate structural features, magnetic properties and hyperthermia performance in these MNPs. The suitability of the seeded-growth approach for the preparation of iron oxide MNPs has been also discussed.

## ■ EXPERIMENTAL SECTION

**Materials.** Iron pentacarbonyl ( $\text{Fe}(\text{CO})_5$ , 98%), oleic acid ( $\text{C}_{17}\text{H}_{33}\text{CO}_2\text{H}$  or OLAC, 90%), oleylamine ( $\text{C}_{17}\text{H}_{33}\text{NH}_2$  or OLAM, 70%), hexadecane-1,2-diol ( $\text{C}_{16}\text{H}_{32}\text{O}_2$  or HDD, technical grade) and 1-octadecene ( $\text{C}_{18}\text{H}_{36}$  or ODE, 90%) were purchased from Aldrich. OLAC, OLAM and ODE were degassed under vacuum at  $120^\circ\text{C}$  for 1 h and stored under nitrogen in a glovebox at  $-20^\circ\text{C}$  before use.

**Synthesis of Iron Oxide MNPs.** Iron oxide MNPs were prepared by a suitably modified literature protocol<sup>38</sup> implemented with a seeded-growth technique.<sup>29,39</sup> The hydrophobic MNPs were transferred in water by following a previously reported polymer coating procedure.<sup>37,40</sup> More details on the synthesis and on the procedure for the transfer of nanoparticles in water can be found in the Supporting Information (SI).

**Dynamic Light Scattering (DLS).** DLS characterization was performed on a Zetasizer Nano ZS90 (Malvern, U.S.) equipped with a 4.0 mW He–Ne laser, operating at 633 nm, and an Avalanche photodiode detector. Measurements were carried out at  $25^\circ\text{C}$ .

**Gel Electrophoresis.** Gel electrophoresis was carried out on a 2% agarose gel, applying a voltage of 100 V for 1 h. Prior to gel loading, a solution of 30% glycerol containing Orange G in gel-loading buffer (corresponding to 20% of the sample loaded volume) was added to each sample.

**Elemental Analysis.** The elemental analysis of the samples was performed by digesting  $25 \mu\text{L}$  of each sample in  $2.5 \text{ mL}$  of aqua regia and 48 h later diluting them to a known volume with miliQ ultrapure water. The measurement was performed with the iCap 6000 Series induced coupled plasma-atomic emission spectroscopy (ICP-AES) instrument from Thermo Fisher.

**X-ray Diffraction (XRD).** XRD spectra were obtained using the Smartlab 9 kW Rigaku diffractometer equipped with a copper rotating

anode. The X-ray source was operated at 40 kV and 150 mA. A Gobel mirror was used to obtain a parallel beam and remove  $\text{CuK}\beta$  radiation (1.392 Å). A flat mirror analyzer was used to remove X-ray fluorescence. A 2theta/omega scan was performed with a step width of  $0.03^\circ$  ( $2\theta$ ) and speed scan of  $0.023^\circ/\text{min}$ .

**Low- and High-Resolution Transmission Electron Microscopy (TEM).** In view of the TEM analysis, a drop of the colloidal solution in toluene or water was deposited onto a thin carbon film supported by a copper TEM grid and then allowing the solvent to evaporate. Low-magnification TEM measurements were carried out with a Jeol JEM-1010 microscope, equipped with a tungsten electron source and working at an acceleration voltage of 100 kV. Statistical analysis was carried out on several wide-field, low-magnification TEM images, with the help of a dedicated software (Gatan Digital Micrograph). For each sample, 200 particles were counted at least. High-resolution TEM (HRTEM) measurements were carried out with a Jeol JEM-2200FS microscope with spherical aberration-corrected objective lens, equipped with a field emission gun (FEG) and working at an acceleration voltage of 200 kV. The HRTEM images were recorded by a Gatan Ultrascan 1000 CCD camera and the structural features of the nanostructures were studied by 2D-Fourier analysis, while the local strain was studied by analyzing the HRTEM images with the peak pair analysis (PPA) method.<sup>41</sup>

**X-ray Absorption Spectroscopy.** X-ray Absorption Near-Edge Structure (XANES) and Extended X-ray Absorption Fine Structure (EXAFS) spectroscopy measurements at the Fe K-edge energy were performed at room temperature in transmission mode at the BM25 Spanish CRG Beamline (SpLine) of the ESRF (European Synchrotron Radiation Facility). Two gas ionization chambers, filled with nitrogen and argon, were used to measure the incident and the transmitted beam, respectively. Powder samples were placed onto a kapton tape located on the beam path. Different quantities of powders were used in the experiments so as to achieve similar signal intensity for all the samples. Several scans were taken, in order to obtain a good signal-to-noise ratio. Bulk metallic Fe, FeO,  $\alpha\text{-Fe}_2\text{O}_3$ ,  $\gamma\text{-Fe}_2\text{O}_3$ , and  $\text{Fe}_3\text{O}_4$  powders were also measured for comparison purposes. Data were normalized applying the same normalization parameters for all the spectra by means of Athena Software.

**Magnetic Measurements.** Magnetization curves of the colloidal suspensions of MNPs ( $[\text{Fe}] \sim 10^{-2} - 10^{-3} \text{ M}$ ) were measured at 300 K as a function of the magnetic field in the range  $0 - 10^4$  Oe using a laboratory-made vibrating magnetometer.<sup>42</sup> Magnetization curves at low temperatures (5 K; from  $-50$  kOe to  $+50$  kOe), and the thermal dependence of the magnetization of liquid samples were also measured in Zero Field Cooling (ZFC) and Field Cooling (FC) runs using a superconducting quantum interference device (SQUID) from Quantum Design. To determine the magnetization per unit volume  $M$ , the net magnetic moment of the suspension was normalized by the total volume of particles, determined from the mass of iron (quantified by ICP-AES) and assuming the spinel crystal structure of magnetite ( $\text{Fe}_3\text{O}_4$ ).

**Hyperthermia Experiments.** The laboratory-made device used for the magnetic hyperthermia experiments was described previously.<sup>9,11</sup> It consists of a resonant RLC circuit producing a 700 kHz magnetic field of  $21 \text{ kA m}^{-1}$  in a coil of 16 mm diameter. The coil is cooled with circulating nonane and the nonane temperature is controlled to reach an equilibrium temperature of  $37^\circ\text{C}$ . The temperature is probed with a fluoro-optic fiber thermometer (Luxtron Corp., CA) and is recorded every 0.7 s after switching on the power supply. The initial linear rise of temperature as a function of time,  $dT(t=0)/dt$ , was measured in order to deduce the power dissipated by one gram of nanoparticles, called the Specific Loss Power (SLP) of the particles, defined as  $\text{SLP} = ((C_V/m)(dT(t=0)/dt))$ , where  $C$  is the volume specific heat capacity of the sample ( $C_{\text{water}} = 4185 \text{ J L}^{-1} \text{ K}^{-1}$ ),  $V_s = 300 \mu\text{L}$  is the sample volume, and  $m$  is the mass of iron oxide.

## RESULTS

**Synthesis of Size-Controlled Iron Oxide MNPs.** Oleate-capped iron oxide nanocrystals with tunable sizes were synthesized by high-temperature decomposition of  $(\text{Fe}(\text{CO})_5)_2$  in a ODE-diluted mixture of OLAC, OLAM and HDD at  $280^\circ\text{C}$ .<sup>38</sup> A one-pot, multistep seeded-growth technique was used to produce MNPs with mean diameter precisely adjustable in the 6–18 nm size range.<sup>29,39</sup> The strategy involved the initial generation of small iron oxide MNP seeds (ca. 6 nm), which could then be grown to progressively larger sizes in the same surfactant environment upon slow supply of extra iron precursor and capping agents. The enlargement of the presynthesized seeds was favored over the formation of new crystal embryos since the energetic cost for the homogeneous nucleation at low supersaturation levels is higher than the one required for the deposition of iron oxide onto the surface of the pre-existing seeds.<sup>43</sup> This mechanism allows the separation of the primary nucleation and secondary growth processes, leading to size-tunable, highly monodisperse MNPs by carefully controlling the relative amount of precursors added to the preformed seeds. The native hydrophobic capping layer of the as-synthesized MNPs was exploited for their transfer into aqueous media following a well-known polymer-coating procedure.<sup>37,40</sup> Amphiphilic polymer molecules (PC14 and PC18) having similar structure but different molecular weight were employed for transferring the nanoparticles into water in order to assess whether the thickness of the polymer layer could affect the heating ability of the magnetic core underneath. Each MNP was enwrapped by polymer molecules that formed a uniform and stable negatively charged shell around the nanoparticles, enabling their solubility into a saline aqueous environment.

**Size and Size Dispersion Studies.** The left column of Figure 1 shows TEM micrographs of seven iron oxide MNP samples with average dimensions ranging from 6 to 18 nm, which were deposited from a toluene solution. The homogeneous and close-packed arrangement of the particles on the TEM grids demonstrates their low degree of size dispersion and the absence of aggregates in the solution. The length of the aliphatic chains of the capping molecules corresponds roughly to half the interparticle distance observed in the images, confirming the efficient role of the surfactants in isolating and stabilizing the MNPs in the organic solution. The size dispersion of all samples was measured over a minimum of 200 particles. In all cases, standard deviation values smaller than 20% with a slight increase with increasing MNP dimensions were deduced. The polymer coating procedure did not affect the monodispersity of MNPs and ensured their homogeneous solubilization in water, as assessed by the TEM micrographs (see the right column of Figure 1) and by DLS measurements (see SI) performed after water transfer. Moreover, the gel electrophoresis of the water-soluble MNPs (Figure S1 of the SI) showed narrow migration bands, confirming the homogeneous size (and charge) distribution of the nanocrystals and evidenced the absence of multiparticle aggregates in solution, regardless of the polymer used.

**Phase Determination.** XRD spectra proved the crystalline nature of all iron oxide samples. The peaks were compared with the diffraction patterns of standard magnetite ( $\text{Fe}_3\text{O}_4$ ) and maghemite ( $\gamma\text{-Fe}_2\text{O}_3$ ) and all matched with the cubic spinel structure even if it was not possible to discern between the two different phases mentioned above. As an example, the X-ray diffraction pattern for 15 nm iron oxide MNPs is shown in Figure 2. It is



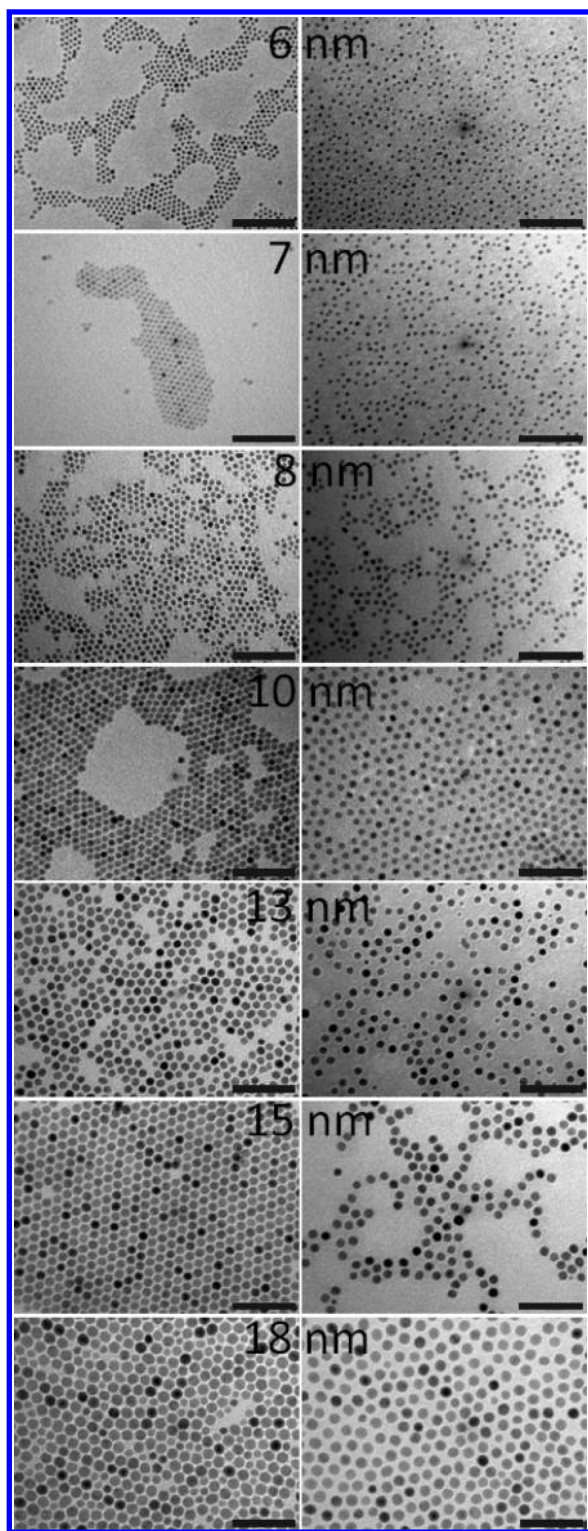


**Figure 1.** TEM micrographs of iron oxide MNPs of different sizes, deposited from organic solvents (left column) and after their transfer to aqueous saline buffer by means of a polymer-coating procedure (right column). On the top of each panel the average size of the particles is indicated in black. The scale bar is marked at the bottom of each micrograph and represents 100 nm in all cases.

well-known that nanostructured materials show diffraction peaks with larger widths with respect to their microstructured or bulk

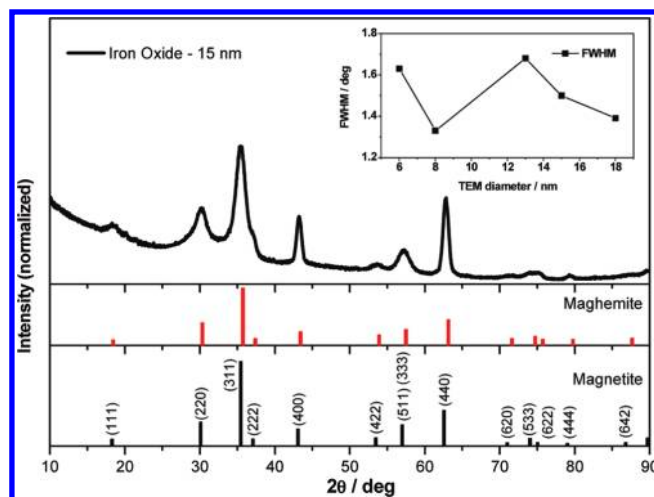


**Figure 2.** X-ray diffraction pattern of iron oxide MNPs with average diameter of 15 nm with the corresponding reference patterns of magnetite and maghemite for comparison. The reflection indexes indicated in the magnetite reference pattern are also valid for the corresponding reflections of the maghemite pattern. The inset shows the evolution of the full width at half-maximum (fwhm) of the peak corresponding to the (311) reflection with the size of the MNPs.

analogues, as expressed in the Scherrer formula.<sup>44,45</sup> However, the peak width should clearly narrow with increasing dimensions. Here we analyzed the size dependence of the full width at half-maximum (fwhm) of the most intense diffraction peak observed for magnetite, corresponding to the (311) reflection (see the inset of Figure 2). As expected, the fwhm decreased by about  $0.4^\circ$  as the MNP size increased from 6 to 8 nm. However, for larger sizes, a significant increase of the fwhm was observed, preliminarily indicating that the larger MNPs could be characterized by a limited length of structural coherence, as assessed in a recent atomic pair distribution function (PDF) analysis of synchrotron XRD patterns collected from iron oxide MNPs synthesized by an analogous approach.<sup>46</sup> The alternative hypothesis of a multidomain polycrystalline structure could be fully discredited on the basis of the results of HRTEM investigations, which will be illustrated in next paragraphs. XANES measurements were performed for all MNP samples in order to get additional structural information and discard the presence of different iron species. As reported in the SI for MNPs of 6 and 18 nm, nanocrystals are composed of pure magnetite regardless of their size.

**High-Resolution TEM measurements.** HRTEM micrographs of 18 nm iron oxide nanoparticles are shown in Figure 3. They revealed homogeneous structures of nanoparticles consistent with a monocrystalline phase as well as the absence of evident lattice defects, such as dislocations or stacking faults. In particular, the numerical electron diffraction patterns (i.e., filtered 2D-FFT) obtained by HRTEM images were compatible with a single-crystal structure as no crystalline reflection splitting or satellite spots were in fact observed in the Fourier space.

**Magnetic Measurements.** Magnetic measurements were performed on both the starting surfactant-coated MNPs and the corresponding water-soluble samples. No significant differences were observed between the surfactant- and polymer-coated analogues. The magnetization of the MNP samples in solution was measured at room temperature as a function of the magnetic field up to  $10^4$  Oe. Volume magnetization curves are represented in Figure 4a for samples of different sizes. The magnetization at

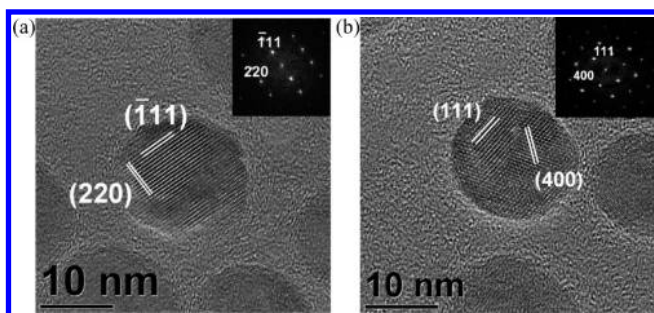


**Figure 3.** HRTEM images of single iron oxide nanocrystals with their corresponding numerical electron diffraction patterns (insets). (a) nanocrystal observed along the  $[1\bar{1}2]$  zone axis, displaying  $(\bar{1}11)$  and  $(220)$  lattice fringes. (b) nanocrystal observed along the  $[01\bar{1}]$  zone axis showing  $(111)$  and  $(400)$  lattice fringes. Numerical electron diffraction patterns are consistent with a monocrystalline phase.

high fields clearly decreased with increasing particle size, this effect being more pronounced above 13 nm. Whereas a plateau was observed for the magnetization of 6–10 nm diameter MNPs, a linear increase of the magnetization was seen at high field strengths (typically above 6 kOe) for larger sizes (see in Figure 4a, the magnetization of the 18 nm sample). The highest magnetization value was found for a particle diameter of 6 nm and was around 55% of the saturation magnetization of the bulk magnetite ( $M_{S \text{ bulk}}$ ). In principle, the decrease of saturation magnetization compared to the bulk material can be explained by the existence of nonfully coordinated atoms at the surface of the particles, leading to the formation of a thin nonferromagnetic or frustrated layer.<sup>34,36,47</sup> Considering nanoparticles with a diameter of 6 nm and a magnetically frustrated layer of 0.5 nm, then only 55% of the nanoparticle volume should actually be effectively ferromagnetic, that is, with an exchange-based order, either ferro- or ferrimagnetic. When the MNP size increases, its surface-to-volume ratio decreases and the saturation magnetization of the particle should approach the bulk value  $M_{S \text{ bulk}}$ . However, Figure 4a shows exactly the opposite trend, according to which the saturation magnetization decreases with increasing MNP size: clearly, the volume that contributes to the overall magnetization of the MNP was smaller than its crystalline volume, the latter being calculated from the average diameter extracted from TEM measurements (henceforth denoted as the TEM diameter) and assuming a spherical geometry. Actually, the ferromagnetic volume fractions ( $\Phi_{\text{FM}}$ ) and a *paramagnetic-like* susceptibility ( $\chi$ ), the latter accounting for the nonsaturating behavior, were calculated for all samples (see details in the SI). The results indicated that  $\Phi_{\text{FM}}$  represented around 55% of the crystal volume for 6 nm particles and further diminished with increasing crystal size. This behavior can be attributed to the presence of a magnetically frustrated phase which does not fully align even at high magnetic fields and which accounts for more than 50% of the total particle volume in most of the samples.

The next step was to deduce the whole distribution of effective ferromagnetic diameters in the solution. This can be achieved by fitting the experimental magnetization curve with a Langevin function weighted by the distribution of ferromagnetic size. To clarify, the normalized magnetization can be written as  $M/M_{\text{max}} = \int P(d_{\text{FM}}) dd_{\text{FM}} L(\zeta_{\text{FM}})$ , where  $M_{\text{max}}$  is the maximum value of the magnetization (from which the eventual “paramagnetic-like” contribution has been subtracted),  $P(d_{\text{FM}})$  is the probability density of a ferromagnetic diameter  $d_{\text{FM}}$ ,  $L(\zeta_{\text{FM}}) = \coth(\zeta_{\text{FM}}) - 1/\zeta_{\text{FM}}$  is

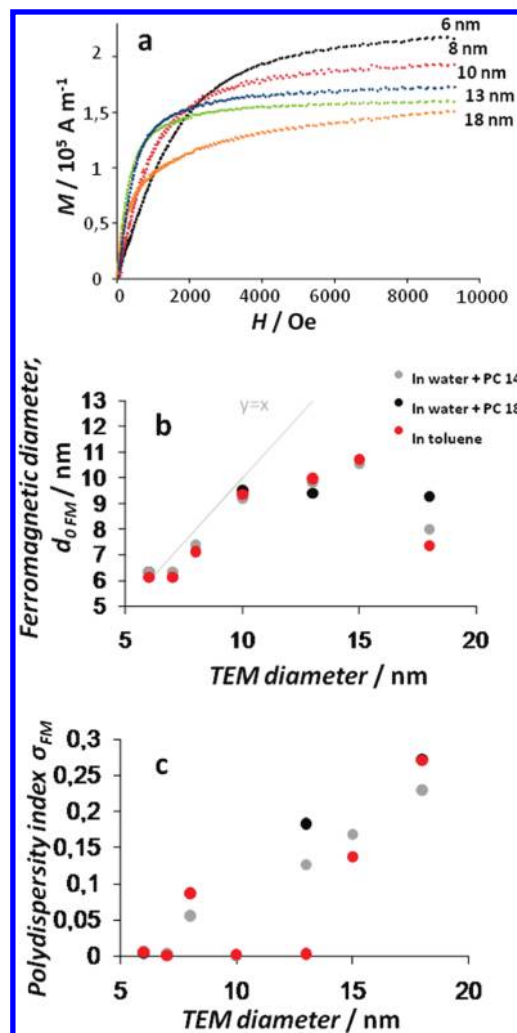


**Figure 4.** (a) Field-dependent magnetization curves of colloidal iron oxide MNPs with different sizes. Ferromagnetic diameters,  $d_{\text{FM}}$ , (b) and magnetic polydispersity indexes,  $\sigma_{\text{FM}}$ , (c) of magnetic size distributions deduced from the fit of the magnetization curves, as a function of TEM diameter.

the Langevin function and  $\zeta_{\text{FM}} = M_{S \text{ bulk}} \pi d_{\text{FM}}^3 \mu_0 H / 6 K_B T$  is the Langevin parameter,  $H$  the applied magnetic field,  $K_B$  the Boltzmann constant and  $T$  the temperature. A log-normal distribution of ferromagnetic diameters,  $P(d_{\text{FM}}) = 1 / ((2\pi)^{1/2} \sigma_{\text{FM}} d_{\text{FM}}) \times \exp(-\ln^2(d_{\text{FM}}/d_{\text{FM0}}) / 2\sigma_{\text{FM}}^2)$ , was found by fitting the experimental curves. The characteristic diameter  $d_{\text{FM0}}$  and polydispersity index  $\sigma_{\text{FM}}$  are shown in Figure 4b–c respectively, as a function of the TEM diameter. Up to a MNP size of 10 nm,  $d_{\text{FM0}}$  is slightly smaller than the TEM diameter and the polydispersity index  $\sigma_{\text{FM}}$  is close to zero, consistent with the uniform sizes observed in TEM micrographs. However, the ferromagnetic diameters diverge from TEM ones and the polydispersity is drastically enhanced for larger particle sizes. Despite their quite homogeneous crystal size, the particles show heterogeneous magnetic behaviors with a high degree of disorder. For 18 nm particles, the ferromagnetic diameter is reduced to 8 nm with a large dispersion and the appearance of a *paramagnetic-like* nonsaturated component of magnetization.

**Hyperthermia Measurements.** To evaluate the efficiency of the iron oxide MNPs as nanomediators for therapeutic hyperthermia, we measured their SLP, expressed in Watts per iron



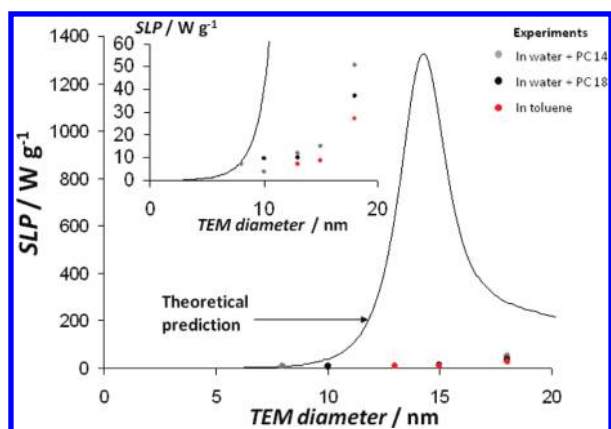


**Figure 5.** Experimental specific loss power (SLP) as a function of TEM diameters for different MNPs dispersed in toluene (red points) or in water (black and gray points). Theoretically predicted SLP values are displayed as a black line for monodisperse magnetite MNPs with a magnetic size equal to the TEM size. The inset represents a zoom on the experimental points.

oxide unit mass (g), in a magnetic field of  $21 \text{ kA m}^{-1}$  oscillating at a frequency of 700 kHz. The measured values are reported in Figure 5 as a function of the TEM diameter. We also represented the theoretical prediction for monodisperse nanoparticles of magnetite.<sup>2</sup> SLPs increased with particle size, but exhibited much lower values than those afforded by MNPs with similar sizes synthesized by coprecipitation.<sup>9</sup> Moreover, the maximum of SLP predicted theoretically for monodisperse 15 nm diameter MNPs was not observed here despite the highly monodisperse crystal sizes and the apparent crystallinity of the MNPs used.

## DISCUSSION

So far, the unusual magnetic behavior and the unexpected low hyperthermia performance exhibited by our MNPs cannot be directly explained by the structural analyses provided by XRD, XAS and HRTEM. For this reason, an in-depth study of these monodisperse, single crystalline and well-dispersed MNPs can shed light on new aspects that could not be otherwise easily disclosed in conventional samples affected by broad size dispersions and/or aggregation phenomena.

**Strain Map Analysis by High Resolution TEM.** Magnetite-like single crystalline MNPs showed no direct evidence of any lattice defect, as reported previously. Starting from HRTEM data and using the analysis method known as peak pairs analysis (PPA), a complete strain tensors study was thus carried out for the 18 nm MNPs in order to identify the presence/absence of strained regions inside the iron oxide monocrystalline structure (more details of the calculations can be found in the SI). The strain maps generated by the mean dilatation, the pure shear and the rigid-body rotation tensor components are shown in Figure 6b–d. In particular, the mean dilatation tensor describes the deformation due to tensile or compressive stress, defined as normal to the body surface; the pure shear tensor describes the deformation due to tangential stress; both the mean dilatation and pure shear tensor are defined so as to give no rotation of the atomic columns. Finally, the rigid body rotation tensor takes into account only the angular rotation component of the atomic columns (see SI for further details). Defective areas are represented by hot spots of blue/red/yellow colors while defect-free areas are represented in green-brown colors.

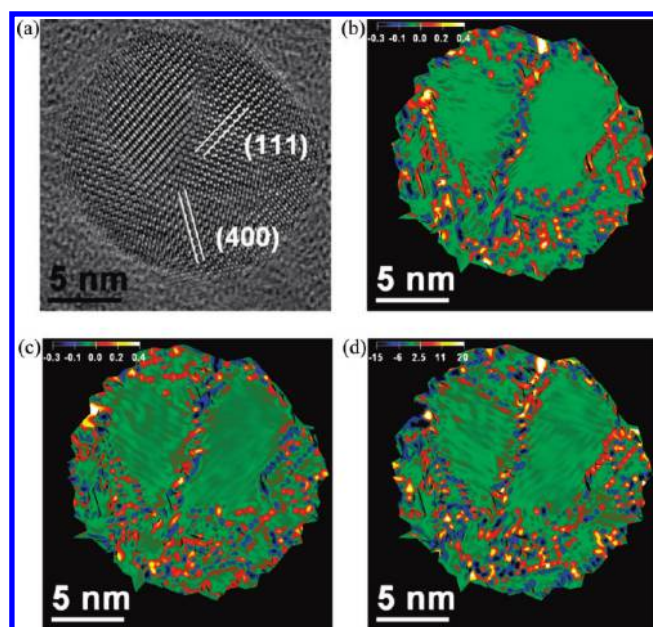


**Figure 6.** Strain maps of a single crystal iron oxide MNP. (a) reference HRTEM image for strain tensor analysis of a spinel ferrite nanocrystal viewed along the  $[01\bar{1}]$  zone axis showing (111) and (400) lattice fringes; (b) mean dilatation strain map; (c) pure shear strain map; (d) rigid-body rotation strain map.

As obtained from strain tensors analysis, a considerable deformation (blue/red/yellow colors in strain maps) is accumulated along some “interfaces” across the nanocrystal and in the external region along a thickness of few nanometers. The strained regions could be considered as a part of the single crystalline domain with a certain degree of structural disorder, even if not enough to give rise to directly observable lattice distortion. This conclusion is consistent with the findings of the aforementioned PDF-synchrotron XRD study recently performed on analogous MNPs, according to which the limited length of structural coherence, which was much smaller than the TEM diameter, was ascribed to lattice strain effects.<sup>46</sup> The results of the strain analysis could provide a first explanation of the anomalous magnetic behavior observed. The alignment of the iron spins could be perturbed in the strained regions. As a consequence, such local lattice distortions could reduce the global magnetic moment of the MNP. Moreover, strained regions are expected to create a strain field spreading across the MNP: magnetic interactions are extremely sensitive to structural changes and hence the structural strain at certain interfaces could easily frustrate the spins along wider regions.

**Low-Temperature Magnetic Analysis.** To highlight the peculiarities of our monodisperse MNPs, we carried out a more systematic study of their field- and temperature-dependent magnetic properties. We focused on the 6 nm MNPs (for which the paramagnetic-like component was absent) and the 18 nm MNPs (for which the paramagnetic-like component was large). Figure 7-top shows the field-dependent magnetization curves measured at 5 K upon field cooling (FC) with  $H_{FC} = 50 \text{ kOe}$  and Zero field cooling (ZFC). For the 6 nm MNPs, the magnetization curves saturate at about 2 kOe. The coercive field at 5 K is 26 Oe. ZFC and FC magnetization curves are very similar although with a 3% difference in magnetization values. On the contrary, the curves corresponding to the 18 nm MNPs exhibit a nonsaturated

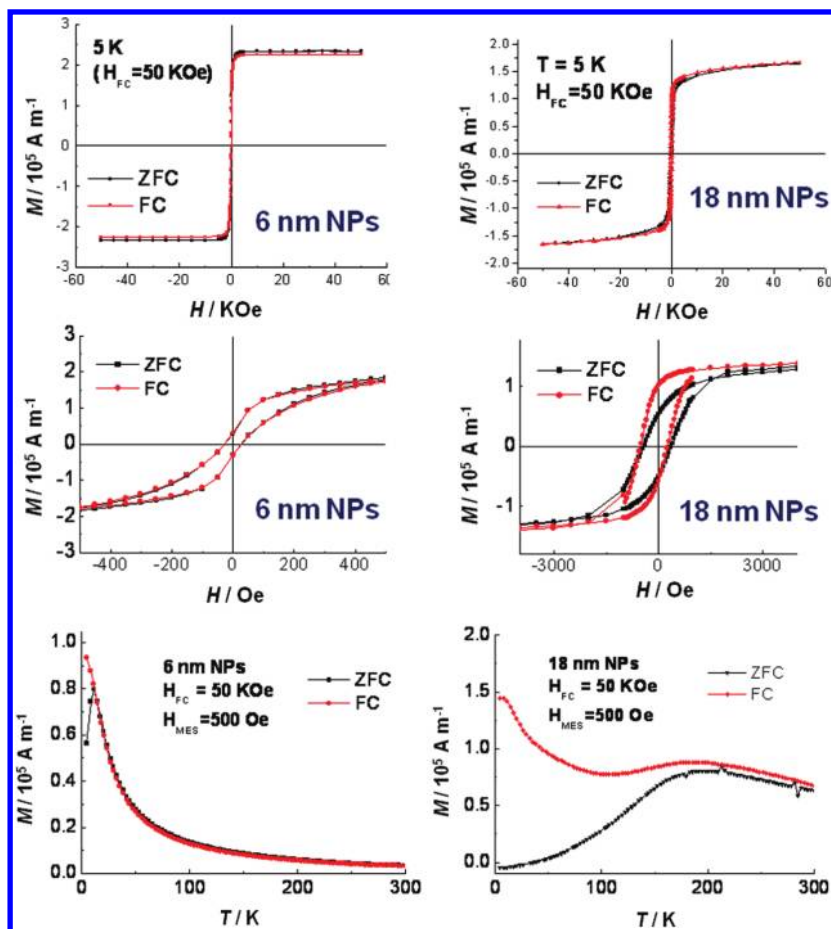


**Figure 7.** Top: Field-dependent magnetization curves for the 6 and 18 nm MNPs at 5 K under ZFC and FC conditions ( $H_{\text{FC}} = 50 \text{ kOe}$ ). Medium: Details of the low field region of the magnetization curves shown at the top. For the 6 nm MNPs, both  $M$  versus  $H$  curves upon FC and ZFC conditions are identical and symmetric with respect to the origin. On the contrary, for the 18 nm MNPs, they are distinct and asymmetric with respect to the origin, showing the features of the exchange bias phenomenon. Bottom: Thermal dependence of the ZFC and FC magnetization for 6 and 18 nm MNPs (the magnetic field applied during cooling is  $H_{\text{FC}} = 50 \text{ kOe}$  while the measuring magnetic field is  $H_{\text{meas}} = 500 \text{ Oe}$ ).

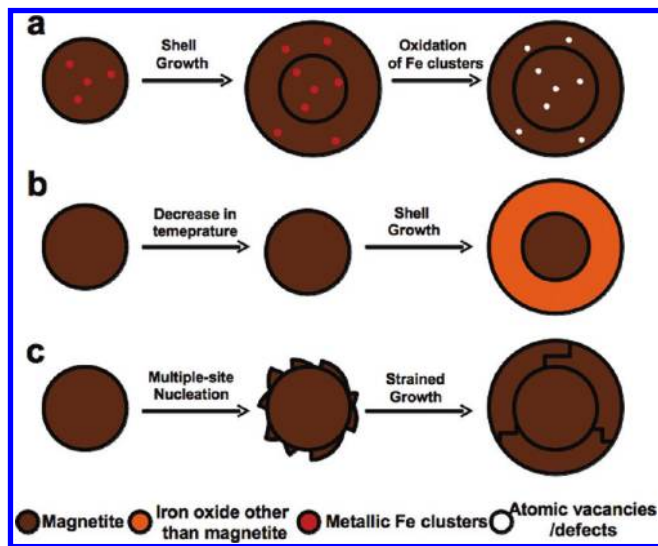
component at 5 K (in a 50 kOe magnetic field). A ferromagnetic phase with Curie temperature ( $T_C$ ) below 300 K would show a paramagnetic behavior at room temperature; however, this behavior would definitely disappear at 5 K, where the ferromagnetic component would undoubtedly be below its  $T_C$ . The fact that we still observe such a nonsaturated magnetization at 5 K indicates that this component is intrinsically nonferromagnetic.

Figure 7-medium presents a detail of the low-field region for the field-dependent magnetization curves at 5 K. For the 6 nm MNPs, ZFC and FC curves are identical. On the contrary, in the case of the 18 nm MNPs, there are significant differences between the ZFC and FC curves. Both magnetization curves show a coercive field of 395 Oe, but are shifted toward negative fields and positive magnetization values, by a field of  $H_{\text{EB}} = 30 \text{ Oe}$  for the ZFC condition and  $H_{\text{EB}} = 126 \text{ Oe}$  for the FC condition. This shift is the fingerprint of exchange bias, a phenomenon that takes place at interfaces between different magnetic phases.<sup>48–50</sup> It is important to remark that the existence of exchange bias phenomena requires the presence of magnetic interfaces into intimate contact and cannot take place between two particles with different magnetic phases through dipolar interactions. Thus, we may conclude that the 18 nm MNPs can be considered as magnetically complex structures, consisting of two phases that correspond to a ferromagnetic phase and a nonsaturated one.

While exchange bias is characteristic of compositionally hybrid structures with domains showing different magnetic behavior (typically ferromagnetic-antiferromagnetic but also ferromagnetic-ferrimagnetic, ferrimagnetic-antiferromagnetic, etc),<sup>48,49,51</sup> it can also appear in simple MNPs with order/disorder interphases. The disorder does not need to be structural but can be a spin disorder such as antiphase boundaries, spin canting or spin glass.<sup>50</sup> It must be noted that the initial seeds of 6 nm do not exhibit this complex behavior. Therefore the exchange bias observed for the larger MNPs is likely due to the features of the growing shell on the initial 6 nm seeds. It turns out that the abnormal magnetic behavior is a consequence of the seeded-growth synthesis method employed here.

The thermal dependence of the magnetization curves, obtained in FC and ZFC runs, for the 6 and 18 nm MNPs is presented in Figure 7-bottom. The 6 nm MNPs exhibit a sharp maximum at the blocking temperature  $T_B = 11 \text{ K}$ . The narrow maximum is consistent with the small size dispersion evidenced by TEM and DLS measurements. The irreversibility temperature, ( $T_{\text{irr}}$ ), corresponding to the temperature where FC and ZFC curves diverge, coincides with  $T_B$ , as expected for monocrystalline and monodisperse superparamagnetic nanoparticles in absence of interparticle interactions. The effective anisotropy constant ( $K$ ) of the 6 nm MNPs was deduced from the equation  $K = 25 K_B T_B / V$ , where  $T_B$  is

**Scheme 1. Possible Mechanisms of Strain Generation in Single-Crystalline Iron Oxide MNPs Grown by a Seeded-Growth Route:** (a) Sporadic Nucleation of Metallic Iron Clusters That Are Later Oxidized to Iron Oxide Can Lead to the Formation of Atomic Vacancies; (b) the Thickness of the Shell As Well As the Lower Temperature at Which This Is Grown Are Likely to Induce Structural Differences between the Two Sections of the MNP; (c) Multiple-Site Nucleation of Iron Oxide Clusters on the Surface of the Seeds, Followed by Their Coalescence to Form a Polycrystalline Thin Shell That Further Grows upon Precursor Injection and Rearranges As a Strained Single Crystal along with the Annealing of the Sample



the blocking temperature, and  $V$  is the volume of the MNP.<sup>34,52</sup>  $K$  was found to be  $5.8 \times 10^4 \text{ J m}^{-3}$  which is fairly larger than the tabulated ones for magnetite.<sup>53</sup> However, it is well-known that iron oxide MNPs exhibit enhanced anisotropy due to the contribution of surface anisotropy that increases significantly for particle sizes below 10 nm.<sup>36</sup> No fingerprint of the Verwey transition, which could account for an increase of anisotropy, is found in the curves.<sup>54</sup> For the 18 nm MNPs, the ZFC curve exhibits a maximum at about 194 K. This maximum is very broad, contrary to the expected behavior for a narrow size distribution of noninteracting particles in solution. The broadening of the ZFC curve is commonly related to the presence of dipolar interactions among nanoparticles, but such interactions do not promote the splitting of  $T_B$  and  $T_{irr}$ , a phenomenon that is associated with the features of individual nanoparticles. By contrast, the maximum of magnetization is found well below the irreversibility temperature  $T_{irr}$  for the 18 nm MNPs, suggesting that this is not a blocking temperature but a freezing transition temperature  $T_g$ . Therefore, in our case, the wide cusp of the ZFC curve is associated with a wide distribution of energy barriers (despite the narrow size distribution) leading to a spread distribution of magnetic frustrations. The frustrated regions would pin the magnetic moment of the ferromagnetic core as evidenced by the appearance of exchange bias, increasing the effective anisotropy of individual MNPs. This increase of the anisotropy would be highly heterogeneous promoting a wide maximum in the ZFC magnetization curve. At this maximum, the inner cores of the nanoparticles become superparamagnetic but the frustrated regions (that

exhibit a much larger irreversibility field) remain blocked. Thus, the difference between FC and ZFC is due to the contribution of magnetically frustrated regions that need larger temperatures to overcome the energy barriers and defrost the magnetic moments.

**Mechanism of Formation of the Magnetic Disorder.** The magnetic and structural features of MNPs are strictly correlated to the synthetic procedure and reagents chosen for their preparation. Three different mechanisms could account for the observed magnetic disorder:

- During the growth of the iron oxide MNPs, and due to the presence in the growth medium of Fe(0) species used as precursors, the partial nucleation of small metallic Fe clusters of a few atoms could take place, which would get enwrapped inside the iron oxide matrix during further growth of the crystal. When the reaction mixture is finally exposed to air at the end of the reaction, these metallic clusters could be easily oxidized leaving behind a significant amount of vacancies or defects. The mechanism is depicted in Scheme 1a.
- Spinel ferrite iron oxide nanoparticles can be found in the form of pure magnetite, pure maghemite or a mixture of the two. The relative amount of the two phases, as well as their spatial distribution in the particle, have been observed to be size-dependent in some cases.<sup>55</sup> In addition, in our case the reaction temperature was decreased by 30 °C for the growth of the shell onto the surface of the 6 nm seeds to avoid the homogeneous nucleation of new iron oxide embryos. Such difference between the temperature at which core and shell were grown could also induce a variation of the oxidation states between the inner and outer sections of the MNPs. The mechanism is depicted in Scheme 1b.
- Alternatively, the highly symmetric cubic lattice of the iron oxide seeds could favor the simultaneous nucleation of iron oxide clusters in multiple sites of the seeds surface upon precursor injection. However, due to the slight differences in surface energy among the different seed facets, together with their different degrees of surfactant coverage, the small iron oxide nuclei forming the shell could initially show different lattice orientations with respect to the seed. Upon further precursor feeding and annealing of the system, the small iron oxide clusters will coalesce forming a single crystalline shell with a clear epitaxy with the seed. Such growth mechanism had already been observed by some of us during the growth of iron oxide domains on *fcc*-FePt nanoparticles.<sup>56</sup> The shell will grow further with time until most of the precursors are consumed. Nevertheless, the presence of highly strained regions in the monocrystalline shell should be taken into consideration due its growth history. This mechanism is depicted in Scheme 1c.

In principle, the three mechanisms are plausible and could take place simultaneously. However, the formation of metallic iron usually requires very low OLAC/Fe(CO)<sub>5</sub> ratios or very high temperatures,<sup>28,30</sup> which is not the case here. In addition, since the 6 nm seeds show the expected magnetic behavior for highly crystalline single domain particles, the mechanism *a* is unlikely to take place because it would also affect the seeds. Instead, mechanisms *b* and *c* are strictly related to the shell growth on the seeds. For a 18 nm nanoparticle with a 6 nm seed, the 12 nm-thick shell represents a 97% of its total volume; thus, and since XANES



measurements provide an average signal over the whole particle, if the crystalline phase of the shell was different to that of the core, the spectrum should result completely different, as it would be basically that of the shell phase. On the contrary we find the XANES spectra for the 6 nm seeds and 18 nm nanoparticles to be almost identical and thus we can conclude that the samples are mainly composed of magnetite regardless of the size of the MNPs. Consequently, mechanism *c* appears to be the most probable one for the formation of the magnetic disorder.

During the second step of the synthesis (overgrowth of additional material layers), a heterogeneous nucleation of several iron oxide clusters can take place over the 6 nm seed. These clusters can grow until they become in contact with each other. Heterogeneous growth can induce a misalignment of the edges among neighboring nucleated clusters, leading to the development of strain at the interfaces. Actually, TEM measurements showed that the strain is accumulated at the facet edges in 18 nm nanoparticles. When the MNP grows, the contact regions increase, enhancing the strain field, and extending it to larger distances of the growing layer to allow for relaxation. Strain is known to induce strong modification of exchange interactions leading to local spin freezing and disorder that results in reduced magnetization and spin disorder.<sup>34,36</sup>

The reduction of magnetization in iron oxide MNPs is a commonly observed effect and thoroughly studied in the literature.<sup>32,34</sup> Particular mechanisms inducing the reduced magnetization—spin canting,<sup>57–59</sup> spin glass,<sup>60</sup> or antiphase boundaries<sup>61–63</sup>—could account for the observed phenomenology. In our case, the volume of magnetically nonsaturated regions increases with the particle size and disappears for particles below the 8 nm size. Thus, we can rule out that the nonsaturated component is due to the surface spin canting or disorder associated with the surface broken symmetry of the particles. Spin glass can also be discarded based on the large shift of the AC susceptibility cusp with the frequency (see SI), which is characteristic of superparamagnetic nanoparticles, in contrast to the weak dependence of the cusp usually observed in spin glass systems.<sup>64</sup>

Antiphase boundaries have been demonstrated to induce magnetic frustration leading to reduced magnetization and exchange bias in  $\text{Fe}_3\text{O}_4$  epitaxial films grown on  $\text{MgO}$ .<sup>61</sup> The magnetic behavior is similar to that described here.  $\text{Fe}_3\text{O}_4$  islands grow heterogeneously and when they become in contact, antiphase boundaries are created, inducing exchange bias and magnetic frustrations. In our case, heterogeneous growth on the different facets of the initial seeds also occurs. Moreover, the shape of the magnetization curves at low temperature upon FC and ZFC (Figure 7) are very similar to that reported for magnetite heterogeneous growth on  $\text{MgO}$ .<sup>61</sup> Thus, antiphase boundaries are likely the reason for the reduced magnetization in these nanoparticles. Besides the existence of structural antiphase boundaries, magnetic boundaries can also be present. In general, iron oxide nanostructures grown by a multistep method (that includes, for instance, coalescence of different domains) keep a kind of magnetic memory effect, which indicates they are complex and that do not exhibit a single domain magnetic behavior.<sup>65,66</sup> The fact that the MNPs are synthesized below their Curie temperature makes difficult to reset this magnetic memory so as to have a single particle-like magnetic behavior.

**Calculation of SLP Values for Iron Oxide MNPs Considering the Effective Magnetic Volumes.** In order to confirm our hypotheses, the theoretical SLP values were recalculated using the linear theory which is valid only for superparamagnetic

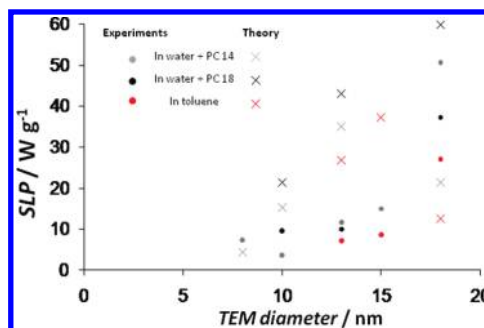


**Figure 8.** The theoretical SLP values, calculated using the magnetic parameters deduced from magnetic fittings shown in Figure 4 and SI Figure S5, are shown for iron oxide samples in water and toluene together with the corresponding experimental values.

nanoparticles and low applied fields. For the calculations, it was taken into account that the SLP depends on the dynamics of the magnetic moment of individual MNPs, subjected to the following relaxation mechanisms: the Brown and the Néel relaxations.<sup>1,2</sup> While the Brownian mechanism depends on the crystal size of the MNP (TEM diameter), the Néel relaxation strictly depends on the ferromagnetic size ( $d_{\text{OFM}}$ ), and no contribution will arise from the *paramagnetic-like* regions. We thus recalculated the theoretical SLP taking the TEM diameter to determine the Brownian relaxation times and the ferromagnetic diameter ( $d_{\text{OFM}}$ ), the ferromagnetic dispersity ( $\sigma_{\text{FM}}$ ) and the ferromagnetic fraction ( $\Phi_{\text{FM}}$ ) to calculate the Néel relaxation times. The anisotropy constant was fixed to  $1.6 \times 10^4 \text{ J m}^{-3}$ , as previously assumed for particles synthesized by coprecipitation method. Consistent with experiments, both the reduced magnetic sizes and the increased magnetic heterogeneity of MNPs with TEM diameters above 13 nm resulted in a drastic decrease of their theoretical SLPs as illustrated in Figure 8. For 15 nm monodisperse particles, a SLP of approximately  $1200 \text{ W g}^{-1}$  is expected if the ferromagnetic volume were equal to the crystal one. Instead, a SLP of  $20 \text{ W g}^{-1}$  was observed and later calculated, consistent with a distribution of ferromagnetic diameters around 10 nm ( $\sigma_{\text{FM}} = 0.15$ ) and a ferromagnetic fraction  $\Phi_{\text{FM}}$  of 0.3.

## CONCLUSIONS

In conclusion, our study offered the possibility to evaluate a set of monodisperse iron oxide MNP samples of different sizes, covering the whole range of dimensions which is expected to be useful for the hyperthermia therapy. In principle, the narrow size distributions of the MNPs, their apparent high crystallinity checked by standard structural techniques and their excellent stability in both organic and aqueous media thanks to a suitable surface functionalization, make these MNPs ideal candidates for the study of their size-dependent hyperthermia performance and for the maximization of heat generation. However, our magnetic study showed the formation of a magnetically frustrated layer in all particles, which increased in dimension with increasing particle size. The heating power of these MNPs was far below the expected value due to a clear discrepancy between the real crystal size and the effective magnetic volume. Magnetic disorder was particularly evident for 13–18 nm MNPs, resulting in a drastic loss of their hyperthermia performance. Compared to previous reports, additional characterization techniques were used in order to understand the characteristics of such dead magnetic layer and correlate them with relevant structural

features. Low-temperature magnetic measurements and strain map analysis of single MNPs indicated the presence of structural and magnetic antiphase boundaries originating from the highly strained crystal lattice of the monocrystalline magnetite MNPs. As a consequence, the effective magnetic volumes of the particles were significantly reduced as well as their magnetic dispersions enlarged. The theoretical SLP values for each sample were recalculated on the basis of the effective magnetic volume of the particles and their magnetic dispersion, thereby obtaining a reasonable agreement with the experiments.

The origin of the crystal strain seems to be strictly related to the two-step seeded-growth synthetic procedure used for their preparation. Generally speaking, the high temperature decomposition of organometallic precursors is a very promising protocol for the preparation of nanoparticles in terms of size and size dispersion control, as well as crystallinity. In particular, the seeded-growth route by which the present MNPs were grown led efficiently to monocrystalline and monodisperse nanocrystals in a wide range of sizes. However, this growth mechanism seems to be responsible for the presence of strained lattice regions which turned out to alter the magnetic structure of the crystals and which could only be detected by highly sensitive techniques. Hence, we highlight here the crucial role of the particular synthetic protocol chosen for the preparation of iron oxide MNPs to be exploited as efficient heat nanomediators for hyperthermia treatments.

MNPs promise to become a powerful tool for cancer therapy in the next few years. However, all the works reported to date indicate SLP values far below the ones theoretically predicted and practically required for the preparation of efficient thermal agents. The heating capacity of MNPs depends on the efficiency of two heating mechanisms, that is, Néel and Brown relaxations, which in turn depend on several structural and magnetic parameters. Hence, the study of MNP-based hyperthermia faces the difficulty of correlating several factors acting simultaneously and which are often difficult to decouple individually. Our work allowed us not only to discriminate among several structural and magnetic features but also to establish correlations among them, which is a fundamental prerequisite to the understanding and development of a new generation of magnetic antitumoral drugs.

## ■ ASSOCIATED CONTENT

**S Supporting Information.** Synthesis of iron oxide MNPs; Transfer of iron oxide MNPs to aqueous solution and conditions used for the purification of the polymer-coated iron oxide MNPs by means of ultracentrifugation; Dynamic light scattering data on iron oxide samples; gel electrophoresis characterization of water-soluble iron oxide MNPs; XANES characterization; analysis of the derivative curves of the X-ray absorption near edge spectra (XANES); X-ray absorption in a wider range of Fe K-edge; Calculation of the ferromagnetic volume fractions ( $\Phi_{\text{FM}}$ ) and apparent paramagnetic-like susceptibilities ( $\chi$ ); Details on the strain analysis by HRTEM; AC susceptibility data of iron oxide MNPs. This material is available free of charge via the Internet at <http://pubs.acs.org>.

## ■ AUTHOR INFORMATION

### Corresponding Author

\*E-mail: [albert.figueroa@qi.ub.es](mailto:albert.figueroa@qi.ub.es) (A. F.); [magarcia@icv.csic.es](mailto:magarcia@icv.csic.es) (M. A. G.).

## ■ ACKNOWLEDGMENT

This work was supported by the European project Magnifyco (Contract NMP4-SL-2009-228622), the Spanish Ministerio de Ciencia e Innovación grants CSD2009-00013, MAT2008-06517-C02-01 and FIS-2008-06249 and Madrid Region Council project NANOBIOMAGNET (S2009/MAT-1726). A.F. acknowledges financial support from the Spanish Government through a Ramón y Cajal Fellowship. We gratefully acknowledge R. Di Corato for assistance with the polymer coating procedure, M. Povia for assistance with XRD measurements, and S. Nitti for assistance with the synthesis of iron oxide MNPs.

## ■ REFERENCES

- (1) Gazeau, F.; Levy, M.; Wilhelm, C. *Nanomedicine* **2008**, *3*, 831.
- (2) Rosensweig, R. E. *J. Magn. Magn. Mater.* **2002**, *252*, 370.
- (3) Ma, M.; Wu, Y.; Zhou, J.; Sun, Y.; Zhang, Y.; Gu, N. *J. Magn. Magn. Mater.* **2004**, *268*, 33.
- (4) Weinstein, J. S.; Varallyay, C. G.; Dosa, E.; Gahramanov, S.; Hamilton, B.; Rooney, W. D.; Muldoon, L. L.; Neuwelt, E. A. *J. Cereb. Blood Flow Metab.* **2010**, *30*, 15.
- (5) Johanssen, M.; Gneveckow, U.; Eckelt, L.; Feussner, A.; Waldo, N.; Scholz, R.; Deger, S.; Wust, P.; Loening, S. A.; Jordan, A. *Int. J. Hyperthermia* **2005**, *21*, 637.
- (6) Foy, S. P.; Manthe, R. L.; Foy, S. T.; Dimitrijevic, S.; Krishnamurthy, N.; Labhasetwar, V. *ACS Nano* **2010**, *4*, 5217.
- (7) Owens, D. E.; Peppas, N. A. *Int. J. Pharm.* **2006**, *307*, 93.
- (8) Figuerola, A.; Di Corato, R.; Manna, L.; Pellegrino, T. *Pharmacol. Res.* **2010**, *62*, 126.
- (9) Fortin, J.-P.; Wilhelm, C.; Servais, J.; Ménager, C.; Bacri, J.-C.; Gazeau, F. *J. Am. Chem. Soc.* **2007**, *129*, 2628.
- (10) Purushotham, S.; Ramanujan, R. V. *J. Appl. Phys.* **2010**, *107*, 114701.
- (11) Levy, M.; Wilhelm, C.; Siaugue, J. M.; Horner, O.; Bacri, J. C.; Gazeau, F. *J. Phys.: Condens. Matter* **2008**, *20*, 509901.
- (12) Gonzales-Weimuller, M.; Zeisberger, M.; Krishnan, K. M. *J. Magn. Magn. Mater.* **2009**, *321*, 1947.
- (13) Dennis, C. L.; Jackson, A. J.; Borchers, J. A.; Hoopes, P. J.; Strawbridge, R.; Foreman, A. R.; Lierop, J. v.; Gruttner, C.; Ivkov, R. *Nanotechnology* **2009**, *20*, 395103.
- (14) Glockl, G.; Hergt, R.; Zeisberger, M.; Dutz, S.; Nagel, S.; Weitschies, W. *J. Phys.: Condens. Matter* **2006**, *18*, S2935.
- (15) Kallumadil, M.; Tada, M.; Nakagawa, T.; Abe, M.; Southern, P.; Pankhurst, Q. A. *J. Magn. Magn. Mater.* **2009**, *321*, 1509.
- (16) Rovers, S. A.; van der Poel, L. A. M.; Dietz, C. H. J. T.; Noijen, J. J.; Hoogenboom, R.; Kemmere, M. F.; Kopinga, K.; Keurentjes, J. T. F. *J. Phys. Chem. C* **2009**, *113*, 14638.
- (17) Rovers, S. A.; Dietz, C. H. J. T.; v. d. Poel, L. A. M.; Hoogenboom, R.; Kemmere, M. F.; Keurentjes, J. T. F. *J. Phys. Chem. C* **2010**, *114*, 8144.
- (18) Büscher, K.; Helm, C. A.; Gross, C.; Glöckl, G.; Romanus, E.; Weitschies, W. *Langmuir* **2004**, *20*, 2435.
- (19) Dennis, C. L.; Jackson, A. J.; Borchers, J. A.; Ivkov, R.; Foreman, A. R.; Lau, J. W.; Goernitz, E.; Gruettner, C. *J. Appl. Phys.* **2008**, *103*, 07A319.
- (20) Chen, S.; Chiang, C.-I.; Hsieh, S. J. *J. Magn. Magn. Mater.* **2010**, *322*, 247.
- (21) Hergt, R.; Dutz, S.; Roder, M. *J. Phys.: Condens. Matter* **2008**, *20*, 385214.
- (22) Hergt, R.; Dutz, S.; Müller, R.; Zeisberger, M. *J. Phys.: Condens. Matter* **2006**, *18*, S2919.
- (23) Frimpong, R. A.; Dou, J.; Pechan, M.; Hilt, J. Z. *J. Magn. Magn. Mater.* **2010**, *322*, 326.
- (24) Kita, E.; Hashimoto, S.; Kayano, T.; Minagawa, M.; Yanagihara, H.; Kishimoto, M.; Yamada, K.; Oda, T.; Ohkohchi, N.; Takagi, T.; Kanamori, T.; Ikehata, Y.; Nagano, I. *J. Appl. Phys.* **2010**, *107*, 09B321.
- (25) Zhao, D. L.; Teng, P.; Xu, Y.; Xia, Q. S.; Tang, J. T. *J. Alloys Compd.* **2010**, *502*, 392.



- (26) Hyeon, T.; Lee, S. S.; Park, J.; Chung, Y.; Na, H. B. *J. Am. Chem. Soc.* **2001**, *123*, 12798.
- (27) Jun, Y.-w.; Huh, Y.-M.; Choi, J.-s.; Lee, J.-H.; Song, H.-T.; KimKim; Yoon, S.; Kim, K.-S.; Shin, J.-S.; Suh, J.-S.; Cheon, J. *J. Am. Chem. Soc.* **2005**, *127*, 5732.
- (28) Park, J.; An, K.; Hwang, Y.; Park, J.-G.; Noh, H.-J.; Kim, J.-Y.; Park, J.-H.; Hwang, N.-M.; Hyeon, T. *Nat. Mater.* **2004**, *3*, 891.
- (29) Sun, S.; Zeng, H. *J. Am. Chem. Soc.* **2002**, *124*, 8204.
- (30) Kwon, S. G.; Hyeon, T. *Acc. Chem. Res.* **2008**, *41*, 1696.
- (31) Jun, Y.-w.; Choi, J.-s.; Cheon, J. *Angew. Chem., Int. Ed.* **2006**, *45*, 3414.
- (32) Guardia, P.; Batlle-Brugal, B.; Roca, A. G.; Iglesias, O.; Morales, M. P.; Serna, C. J.; Labarta, A.; Batlle, X. *J. Magn. Magn. Mater.* **2007**, *316*, e756.
- (33) Roca, A. G.; Niznansky, D.; Poltierova-Vejpravova, J.; Bittova, B.; Gonzalez-Fernandez, M. A.; Serna, C. J.; Morales, M. P. *J. Appl. Phys.* **2009**, *105*, 114309.
- (34) Batlle, X.; Labarta, A. *J. Phys. D: Appl. Phys.* **2002**, *35*, R15.
- (35) Tronc, E.; Fiorani, D.; Noguès, M.; Testa, A. M.; Lucari, F.; D'Orazio, F.; Grenèche, J. M.; Wernsdorfer, W.; Galvez, N.; Chanéac, C.; Mailly, D.; Jolivet, J. P. *J. Magn. Magn. Mater.* **2003**, *262*, 6.
- (36) Shendruk, T. N.; Desautels, R. D.; Southern, B. W.; van Lierop, J. *Nanotechnology* **2007**, *18*, 455704.
- (37) Pellegrino, T.; Manna, L.; Kudera, S.; Liedl, T.; Koktysh, D.; Rogach, A. L.; Keller, S.; Rädler, J.; Natile, G.; Parak, W. J. *Nano Lett.* **2004**, *4*, 703.
- (38) Cozzoli, P. D.; Snoeck, E.; Garcia, M. A.; Giannini, C.; Guagliardi, A.; Cervellino, A.; Gozzo, F.; Hernando, A.; Achterhold, K.; Ciobanu, N.; Parak, F. G.; Cingolani, R.; Manna, L. *Nano Lett.* **2006**, *6*, 1966.
- (39) Park, J.; Lee, E.; Hwang, N.-M.; Kang, M.; Kim, S. C.; Hwang, Y.; Park, J.-G.; Noh, H.-J.; Kim, J.-Y.; Park, J.-H.; Hyeon, T. *Angew. Chem., Int. Ed.* **2005**, *44*, 2872.
- (40) Di Corato, R.; Quarta, A.; Piacenza, P.; Ragusa, A.; Figuerola, A.; Buonsanti, R.; Cingolani, R.; Manna, L.; Pellegrino, T. *J. Mater. Chem.* **2008**, *18*, 1991.
- (41) Galindo, P. L.; Kret, S.; Sanchez, A. M.; Laval, J. Y.; Yanez, A.; Pizarro, J.; Guerrero, E.; Ben, T.; Molina, S. I. *Ultramicroscopy* **2007**, *107*, 1186.
- (42) Bacri, J. C.; Perzynski, R.; Salin, D.; Cabuil, V.; Massart, R. *J. Magn. Magn. Mater.* **1986**, *62*, 36.
- (43) Yu, H.; Gibbons, P. C.; Kelton, K. F.; Buhro, W. E. *J. Am. Chem. Soc.* **2001**, *123*, 9198.
- (44) Klug, H. P.; Alexander, L. E. *X-ray Diffraction Procedures for Polycrystalline and Amorphous Materials*; John Wiley & Sons: New York, 1962.
- (45) Cullity, B. D.; Stock, S. R. *Elements of X-Ray Diffraction*; 3rd ed.; Prentice-Hall Inc.: New York, 2001.
- (46) Petkov, V.; Cozzoli, P. D.; Buonsanti, R.; Cingolani, R.; Ren, Y. *J. Am. Chem. Soc.* **2009**, *131*, 14264.
- (47) Kim, T.; Shima, M. *J. Appl. Phys.* **2007**, *101*, 09M516.
- (48) Nogues, J.; Schuller, I. K. *J. Magn. Magn. Mater.* **1999**, *192*, 203.
- (49) Nogues, J.; Sort, J.; Langlais, V.; Skumryev, V.; Surinach, S.; Munoz, J. S.; Baro, M. D. *Phys. Rep.* **2005**, *422*, 65.
- (50) Iglesias, O.; Labarta, A.; Batlle, X. *J. Nanosci. Nanotechnol.* **2008**, *8*, 2761.
- (51) Casavola, M.; Falqui, A.; Garcia, M. A.; García-Hernández, M.; Giannini, C.; Cingolani, R.; Cozzoli, P. D. *Nano Lett.* **2009**, *9*, 366.
- (52) Caruntu, D.; Caruntu, G.; O'Connor, C. J. *J. Phys. D: Appl. Phys.* **2007**, *40*, 5801.
- (53) Bickford, L. R. *J. Phys. Rev.* **1950**, *78*, 449.
- (54) Walz, F. *J. Phys.: Condens. Matter* **2002**, *14*, R285.
- (55) Santoyo Salazar, J.; Perez, L.; de Abril, O.; Phuoc, L. T.; Ithiawakrim, D.; Vazquez, M.; Greneche, J.-M.; Begin-Colin, S.; Pourroy, G. *Chem. Mater.* **2011**, *23*, 1379.
- (56) Figuerola, A.; Fiore, A.; Di Corato, R.; Falqui, A.; Giannini, C.; Micotti, E.; Lascialfari, A.; Corti, M.; Cingolani, R.; Pellegrino, T.; Cozzoli, P. D.; Manna, L. *J. Am. Chem. Soc.* **2008**, *130*, 1477.
- (57) Pankhurst, Q. A.; Pollard, R. J. *Phys. Rev. Lett.* **1991**, *67*, 248.
- (58) Morales, M. P.; Veintemillas-Verdaguer, S.; Montero, M. I.; Serna, C. J.; Roig, A.; Casas, L.; Martinez, B.; Sandiumenge, F. *Chem. Mater.* **1999**, *11*, 3058.
- (59) Linderroth, S.; Hendriksen, P. V.; Bodker, F.; Wells, S.; Davies, K.; Charles, S. W.; Morup, S. *J. Appl. Phys.* **1994**, *75*, 6583.
- (60) Mydosh, J. A. *J. Magn. Magn. Mater.* **1978**, *7*, 237.
- (61) Arora, S. K.; Sofin, R. G. S.; Nolan, A.; Shvets, I. V. *J. Magn. Magn. Mater.* **2005**, *286*, 463.
- (62) Novakova, A. A.; Lanchinskaya, V. Y.; Volkov, A. V.; Gendler, T. S.; Kiseleva, T. Y.; Moskvina, M. A.; Zevin, S. B. *J. Magn. Magn. Mater.* **2003**, *258*, 354.
- (63) Margulies, D. T.; Parker, F. T.; Rudee, M. L.; Spada, F. E.; Chapman, J. N.; Aitchison, P. R.; Berkowitz, A. E. *Phys. Rev. Lett.* **1997**, *79*, 5162.
- (64) Mulder, C. A. M.; van Duynveldt, A. J.; Mydosh, J. A. *Phys. Rev. B* **1981**, *23*, 1384.
- (65) Morales, M. P.; Gonzalez-Carreño, T.; Serna, C. J. *J. Mater. Res.* **1992**, *7*, 2538.
- (66) Stachen, M.; Morales, M. P.; Ocan, M.; Serna, C. J. *Phys. Chem. Chem. Phys.* **1999**, *1*, 4465.